Springer

Acta Mechanica Sinica

CrossMark click for updates

•RESEARCH PAPER•

Acta Mech. Sin., Vol. 38, 421439 (2022)
https://doi.org/10.1007/s10409-022-21439-2

Fracture analysis of a plane crack problem under chemo-mechanical loading

Juntao Shi[1], and Zheng Zhong[1,2*]

[1] *School of Aerospace Engineering and Applied Mechanics, Tongji University, Shanghai 200092, China;*
[2] *School of Science, Harbin Institute of Technology, Shenzhen 518055, China*

Received February 2, 2022; accepted March 3, 2022; published online April 7, 2022

Fracture analysis of a plane crack problem under chemo-mechanical loading is presented based on a linear chemo-elasticity model. The flux conductivity is introduced to characterize the influence of the crack defect on the diffusion process. Using Fourier transform and the dislocation density functions, the crack problem is reduced to a set of singular integral equations, which are solved numerically by the Lobatto-Chebyshev method. Parametric studies are conducted to reveal the effects of flux conductivity, geometric configuration, chemical and mechanical loads on the crack tip field. The numerical results show that the stress singularity at the crack tip is usually a mixture of mode I and mode II types.

Chemo-mechanical coupling, Plane crack, Singular integral equations, Stress intensity factor

Citation: J. Shi, and Z. Zhong, Fracture analysis of a plane crack problem under chemo-mechanical loading, Acta Mech. Sin. **38**, 421439 (2022), https://doi.org/10.1007/s10409-022-21439-2

1. Introduction

Chemo-mechanical coupling is common in the complex behavior of natural porous media [1], biological tissues, advanced functional materials [2], and energy conversion and storage devices [3,4]. The transfer and transformation of mass, momentum, and energy will occur under various stimuli such as temperature [5], pH [6], light [7], chemical reaction [8], chemical potential, and stress. In general, there are two mechanisms for mass transfer of fluids in media [9]: Darcy's law, i.e., pressure-driven diffusion [10], such as the consolidation process of clay and fluid seepage in oil/gas extraction; and Fick's law, i.e., chemical potential driven diffusion [11,12], such as ion diffusion in polymers and biological materials.

Chemo-elasticity mainly refers to the coupled theory of diffusion and deformation in elastic solids. Generally, it is necessary to solve the mass conservation equation coupled with strain (or stress) and the elasticity equations considering the diffusion effect. Currently, finite element methods are mainly used to obtain numerical solutions [13-16]. Only some studies have given analytical solutions or asymptotic solutions under equilibrium or some other special cases. Christensen and Newman [17] studied the one-dimensional volume expansion and contraction and stress distribution problems, which are arisen from lithium intercalation in electrode spherical particles. The asymptotic perturbation methods are used to analyze the two-dimensional chemo-elasticity problems under chemical equilibrium, such as a circular hole in an infinite plate, a straight edge dislocation [18], and a circular nano-hole in a large thick plate [19]. Further, Bishay et al. [20] developed a perturbation finite element formulation to analyze chemo-elastic boundary value problems under chemical equilibrium, exemplified in several cases such as plates with elliptical holes and cracks. Xu et al. [21] studied the degradation of materials due to exposure to chemical species and temperature, and obtained semi-analytical solutions of spherical shells, beams, and cylindrical structures under the quasi-static state. Recently, Zhang and Zhong [22,23] developed a continuum theoretical framework of coupled deformation, mass diffusion, heat conduction, and chemical reaction for chemically

*Corresponding author. E-mail address: zhongk@tongji.edu.cn (Zheng Zhong)
Executive Editor: Jianxiang Wang

active solids. And they formulated a generalized isotropic linear theory of chemo-elasticity at isothermal conditions. Numerical cases of transient swelling accompanied by the chemical reaction of a polymer membrane were analyzed. Zhong et al. [24] studied a gel with moisture absorption and hydrolysis reaction by using the above model and predicted the chemo-mechanical responses at the transient and steady states.

At present, there are also some studies on crack problems considering chemical-mechanical coupling. Haftbaradaran and Qu [25] constructed the path-independent J-integral under electrochemical equilibrium and solved the problem of a thin elastic film delaminated from a thick elastic substrate. Zhang et al. [26] presented J-integral and L-integral under electrochemical equilibrium based on Noether's theorem, and the path-independent integrals can provide a practical tool for numerical evaluation of singular fields. In a recent paper, Yang and Qu [8] conducted molecular dynamics simulations to obtain the material properties and critical fracture strain, and then calculated the concentration and stress-strain fields using an implicit procedure in ABAQUS based on a continuum chemo-mechanical model. However, most available work only considered the crack problems under chemical equilibrium states, and comparatively few studies focused on the crack problems under steady or transient chemical processes.

Hence, in this paper, we are devoted to studying the coupling chemical and mechanical fields near a crack under steady state diffusion. The paper is organized as follows. Section 2 summarizes the governing equations for plane strain cases under steady state diffusion and describes an equivalent decomposition of the original crack problem. In Sect. 3, the Fourier transform is used to derive the singular integral equations corresponding to the crack problem in terms of the dislocation density functions. The field quantities near the crack are analyzed in Sect. 4. In Sect. 5, parametric studies are conducted for the chemical potential and stress intensity factors. Section 6 concludes the present study with a summary.

2. Problem formulation

2.1 Governing equations

Consider a chemically active body made of an elastic host solid and a diffusive species coming from outside. For two-dimensional plane problems, we assume that all field quantities are only functions of x and y, that is

$$u = u(x,y),\ v = v(x,y),\ c = c(x,y), \tag{1}$$

where u and v are respectively the displacement components along x-axis and y-axis directions, and c is the concentration of the diffusive species (defined by the molar number of molecules per unit volume). Furthermore, for a plane strain problem, the linear strain components are given as

$$\begin{aligned} &\varepsilon_x = \frac{\partial u}{\partial x},\ \varepsilon_y = \frac{\partial v}{\partial y},\ \varepsilon_{xy} = \frac{1}{2}\left(\frac{\partial u}{\partial y} + \frac{\partial v}{\partial x}\right), \\ &\varepsilon_z = \varepsilon_{yz} = \varepsilon_{xz} = 0. \end{aligned} \tag{2}$$

Assume that the host solid is an isotropic and linearly elastic material, whose material properties will not change during the species diffusion process. The components of the Cauchy stress tensor in the chemically active material are related to the strains and concentration as [12,23]

$$\begin{aligned} \sigma_x &= \lambda\left(\varepsilon_x + \varepsilon_y\right) + 2G\varepsilon_x - 3\eta K(c - c_0), \\ \sigma_y &= \lambda\left(\varepsilon_x + \varepsilon_y\right) + 2G\varepsilon_y - 3\eta K(c - c_0), \\ \sigma_z &= \lambda\left(\varepsilon_x + \varepsilon_y\right) - 3\eta K(c - c_0), \\ \sigma_{xy} &= 2G\varepsilon_{xy},\ \ \sigma_{xz} = \sigma_{yz} = 0, \end{aligned} \tag{3}$$

where λ, G, and K are respectively the Lame constant, shear modulus, and bulk modulus of the material with $K = 3\lambda + 2G$, η is the coefficient of chemical expansion, and c_0 is the reference concentration in the initial state which is taken to be stress-free, and has a reference chemical potential μ_0. In the absence of body forces, the stress components need to satisfy the following equilibrium equations:

$$\frac{\partial \sigma_x}{\partial x} + \frac{\partial \sigma_{xy}}{\partial y} = 0,\ \frac{\partial \sigma_{xy}}{\partial x} + \frac{\partial \sigma_y}{\partial y} = 0. \tag{4}$$

The chemical potential can be given as [12]

$$\mu - \mu_0 = N(c - c_0) - 3\eta K\left(\varepsilon_x + \varepsilon_y\right), \tag{5}$$

where N is the chemistry modulus and $\hat{\mu} = \mu - \mu_0$ is defined as the chemical potential difference. Although in many cases, the chemical potential can be described by a logarithmic function of the concentration, a linear approximation can also be used in some cases [12,23,27,28]. The linear model is easy for theoretical analysis by invoking superposition principle so that it is employed as the first step in tackling many complex muti-physics problems. When the body reaches a state of chemical equilibrium, the chemical potential will remain constant and distribute uniformly everywhere. In a steady or transient state, however, the driving force for diffusion is the gradient of chemical potential, and the diffusion flux will follow a generalized Fick's law [12,27,28]:

$$j_x = -D_m\frac{\partial \hat{\mu}}{\partial x},\ j_y = -D_m\frac{\partial \hat{\mu}}{\partial y}, \tag{6}$$

where j_x and j_y are two flux components, and D_m is constant fluid mobility. The mass balance for the diffusive species should be written as $\frac{\partial c}{\partial t} = -\frac{\partial j_x}{\partial x} - \frac{\partial j_y}{\partial y}$. Under steady state diffusion, the mass balance equation becomes

$$\frac{\partial^2 \hat{\mu}}{\partial x^2} + \frac{\partial^2 \hat{\mu}}{\partial y^2} = 0. \tag{7}$$

Substituting Eq. (5) into Eq. (3), we can rewrite the stress components as

$$\begin{aligned}\sigma_x &= \lambda_c\left(\varepsilon_x+\varepsilon_y\right)+2G\varepsilon_x-\frac{3\eta K}{N}\hat{\mu},\\ \sigma_y &= \lambda_c\left(\varepsilon_x+\varepsilon_y\right)+2G\varepsilon_y-\frac{3\eta K}{N}\hat{\mu},\\ \sigma_{xy} &= 2G\varepsilon_{xy},\end{aligned} \tag{8}$$

where $\lambda_c = \lambda - 9\eta^2K^2/N$. With the help of Eqs. (2), (4), and (8), we can obtain the governing equations:

$$\begin{aligned}\left(\lambda_c+2G\right)\frac{\partial^2 u}{\partial x^2}+\left(\lambda_c+G\right)\frac{\partial^2 v}{\partial x\partial y}+G\frac{\partial^2 u}{\partial y^2} &= \frac{3\eta K}{N}\frac{\partial\hat{\mu}}{\partial x},\\ \left(\lambda_c+2G\right)\frac{\partial^2 v}{\partial y^2}+\left(\lambda_c+G\right)\frac{\partial^2 u}{\partial x\partial y}+G\frac{\partial^2 v}{\partial x^2} &= \frac{3\eta K}{N}\frac{\partial\hat{\mu}}{\partial y}.\end{aligned} \tag{9}$$

As shown in Fig. 1, a strip contains a crack of length $2l$. The crack face is along the x-axis direction, and the midpoint of the crack is taken as the coordinate origin. The thickness of the upper and lower layers are a and b, respectively. The chemical potential differences on the upper and lower surfaces of the strip are kept constant, given by $\hat{\mu}_b$ and $\hat{\mu}_a$ (assume $\hat{\mu}_b > \hat{\mu}_a$). The normal stress and shear stress on the strip surfaces are $p_0(x)$ and $q_0(x)$, respectively.

The superscripts "+" and "−" are used to denote the field quantities for $y > 0$ and $y < 0$, respectively. On the crack face, the two extreme diffusion boundary conditions are the fully impermeable,

$$\frac{\partial\hat{\mu}^+(x,0)}{\partial y} = \frac{\partial\hat{\mu}^-(x,0)}{\partial y} = 0,\ |x| < l, \tag{10}$$

and the fully permeable,

$$\hat{\mu}^+(x,0) = \hat{\mu}^-(x,0),\ \frac{\partial\hat{\mu}^+(x,0)}{\partial y} = \frac{\partial\hat{\mu}^-(x,0)}{\partial y},\ |x| < l. \tag{11}$$

In the fully permeable case, the chemical potential distribution problem is solved by simply ignoring the crack. Thus, the diffusion flux can be obtained as

$$j_{xc} = 0,\ j_{yc} = -D_m j_0, \tag{12}$$

where $j_0 = \dfrac{\hat{\mu}_b-\hat{\mu}_a}{a+b}$.

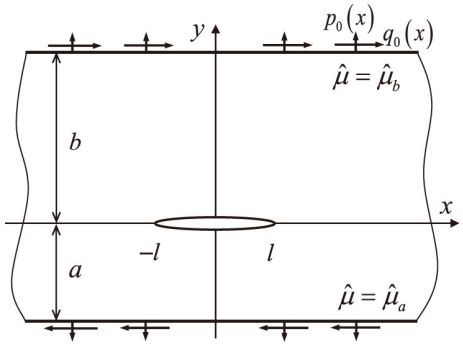

Figure 1 Geometry and loads of a plane crack problem.

The actual diffusion boundary conditions on the crack face are much more complex than those given by Eqs. (10) and (11). And a more general model is adopted in this study, with an assumption that the crack allows a diffusion flux j_y which is only a certain percentage of the flux j_{yc} corresponding to the fully permeable case [29]. Therefore, these partial conductive boundary conditions on the crack faces can be written as

$$\frac{\partial\hat{\mu}^+(x,0)}{\partial y} = \frac{\partial\hat{\mu}^-(x,0)}{\partial y} = k^*j_0,\ |x| < l, \tag{13}$$

where $k^* \in [0, 1]$ is the flux conductivity for the crack, which characterizes the influence of the crack defect on the diffusion process. The limiting case $k^* = 0$ represents the fully impermeable condition along the crack face. While for $k^* = 1$, the diffusion flux on crack face is the same as the fully permeable case, so the boundary condition Eq. (13) is equivalent to Eq. (11).

The boundary conditions of the problem shown in Fig. 1 can thus be written as

$$\begin{aligned}&\sigma_y^+(x,b) = \sigma_y^-(x,-a) = p_0(x),\\ &\sigma_{xy}^+(x,b) = \sigma_{xy}^-(x,-a) = q_0(x),\ |x| < \infty,\end{aligned} \tag{14}$$

$$\begin{aligned}\sigma_y^+(x,0) &= \sigma_{xy}^+(x,0)\\ &= \sigma_y^-(x,0) = \sigma_{xy}^-(x,0) = 0,\ |x| < l,\end{aligned} \tag{15}$$

$$\hat{\mu}^+(x,b) = \hat{\mu}_b,\ \hat{\mu}^-(x,-a) = \hat{\mu}_a,\ |x| < \infty, \tag{16}$$

$$\frac{\partial\hat{\mu}^+(x,0)}{\partial y} = \frac{\partial\hat{\mu}^-(x,0)}{\partial y} = k^*j_0,\ |x| < l. \tag{17}$$

2.2 Superposition principle

For a small deformation case with linear constitutive relations, the superposition principle can be applied. As shown in Fig. 2, the original crack problem is further decomposed into two subproblems with the following equivalent superposition conditions:

$$u = u^{\mathrm{I}} + u^{\mathrm{II}},\ v = v^{\mathrm{I}} + v^{\mathrm{II}},\ \hat{\mu} = \hat{\mu}^{\mathrm{I}} + \hat{\mu}^{\mathrm{II}}, \tag{18}$$

where the superscripts "I" and "II" denote the field quantities of subproblem I and subproblem II, respectively.

Subproblem I As shown in Fig. 2a, the uncracked strip is subjected to the same external loads as the original problem. Under a steady state, there is a diffusion flux $J_0 = j_{yc}$ in the strip. The normal stress and shear stress across the dotted line ($|x| < l, y = 0$) are $p(x)$ and $q(x)$, respectively. The boundary conditions of subproblem I can be written as

$$\begin{aligned}&\sigma_y^{\mathrm{I}+}(x,b) = \sigma_y^{\mathrm{I}-}(x,-a) = p_0(x),\\ &\sigma_{xy}^{\mathrm{I}+}(x,b) = \sigma_{xy}^{\mathrm{I}-}(x,-a) = q_0(x),\ |x| < \infty,\end{aligned} \tag{19}$$

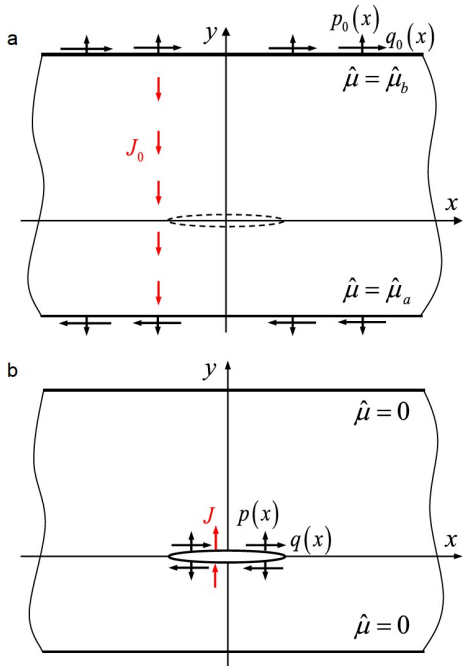

Figure 2 Geometry and loads of two subproblems: **a** subproblem I, **b** subproblem II.

$$\hat{\mu}^{\mathrm{I}+}(x,b)=\hat{\mu}_b,\ \hat{\mu}^{\mathrm{I}-}(x,-a)=\hat{\mu}_a,\ |x|<\infty. \tag{20}$$

And the distribution of chemical potential difference in the strip is $\hat{\mu}^{\mathrm{I}}=\dfrac{\hat{\mu}_b-\hat{\mu}_a}{a+b}y+\dfrac{a\hat{\mu}_b+b\hat{\mu}_a}{a+b}$.

Subproblem II As shown in Fig. 2b, both the chemical and mechanical loads on the strip surfaces vanish. The applied crack face normal stress and shear stress are $-p(x)$ and $-q(x)$. The sum of the crack face flux J and the flux J_0 should be the same as Eq. (13), so that $J=(k^*-1)j_{yc}$. The detailed solutions of this subproblem will be given in the next section.

3. Subproblem II: loads on the crack face

For convenience, although not labeled, the field quantities discussed in this section are for subproblem II. The corresponding mechanical boundary and continuity conditions are expressed as

$$\begin{aligned}\sigma_y^+(x,b)&=\sigma_{xy}^+(x,b)\\&=\sigma_y^-(x,-a)=\sigma_{xy}^-(x,-a)=0,\ |x|<\infty,\end{aligned} \tag{21}$$

$$\sigma_y^+(x,0)=\sigma_y^-(x,0),\ \sigma_{xy}^+(x,0)=\sigma_{xy}^-(x,0),\ |x|<\infty, \tag{22}$$

$$u^+(x,0)=u^-(x,0),\ v^+(x,0)=v^-(x,0),\ |x|\geq l, \tag{23}$$

$$\sigma_y^+(x,0)=-p(x),\ \sigma_{xy}^+(x,0)=-q(x),\ |x|<l, \tag{24}$$

and the chemical boundary conditions are given by

$$\hat{\mu}^+(x,b)=\hat{\mu}^-(x,-a)=0,\ |x|<\infty, \tag{25}$$

$$\frac{\partial\hat{\mu}^+(x,0)}{\partial y}=\frac{\partial\hat{\mu}^-(x,0)}{\partial y},\ |x|<\infty, \tag{26}$$

$$\hat{\mu}^+(x,0)=\hat{\mu}^-(x,0),\ |x|\geq l, \tag{27}$$

$$\frac{\partial\hat{\mu}^+(x,0)}{\partial y}=(k^*-1)j_0,\ |x|<l. \tag{28}$$

3.1 General solutions

The Fourier transform can be used to transform partial differential equations (7) and (9) into a system of ordinary differential equations, as follows:

$$-\omega^2M+\frac{\partial^2M}{\partial y^2}=0, \tag{29}$$

$$\begin{aligned}&-\omega^2(\lambda_c+2G)U+\mathrm{i}\omega(\lambda_c+G)\frac{\partial V}{\partial y}+G\frac{\partial^2U}{\partial y^2}=\mathrm{i}\omega\frac{3\eta K}{N}M,\\&(\lambda_c+2G)\frac{\partial^2V}{\partial y^2}+\mathrm{i}\omega(\lambda_c+G)\frac{\partial U}{\partial y}-\omega^2GV=\frac{3\eta K}{N}\frac{\partial M}{\partial y},\end{aligned} \tag{30}$$

where "i" is the imaginary unit. The Fourier transform and inverse Fourier transform are given by

$$\begin{cases}M(\omega,y)=\dfrac{1}{2\pi}\displaystyle\int_{-\infty}^{\infty}\hat{\mu}(x,y)\mathrm{e}^{-\mathrm{i}\omega x}\mathrm{d}x,\\U(\omega,y)=\dfrac{1}{2\pi}\displaystyle\int_{-\infty}^{\infty}u(x,y)\mathrm{e}^{-\mathrm{i}\omega x}\mathrm{d}x,\\V(\omega,y)=\dfrac{1}{2\pi}\displaystyle\int_{-\infty}^{\infty}v(x,y)\mathrm{e}^{-\mathrm{i}\omega x}\mathrm{d}x,\end{cases}\quad\begin{cases}\hat{\mu}(x,y)=\displaystyle\int_{-\infty}^{\infty}M(\omega,y)\mathrm{e}^{\mathrm{i}\omega x}\mathrm{d}\omega,\\u(x,y)=\displaystyle\int_{-\infty}^{\infty}U(\omega,y)\mathrm{e}^{\mathrm{i}\omega x}\mathrm{d}\omega,\\v(x,y)=\displaystyle\int_{-\infty}^{\infty}V(\omega,y)\mathrm{e}^{\mathrm{i}\omega x}\mathrm{d}\omega.\end{cases} \tag{31}$$

Then, the general solution of Eq. (29) may be expressed as linear combinations of fundamental solutions:

$$M^{\pm}(\omega,y)=\sum_{n=1}^{2}B_n^{\pm}(\omega)M_n, \tag{32}$$

where $B_n^{\pm}(\omega)(n=1,2)$ are unknown functions, and the fundamental solutions are $M_1=\mathrm{e}^{-\omega y}$, $M_2=\mathrm{e}^{\omega y}$. According to Eq. (25), we obtain the general solution of chemical potential using the inverse Fourier transform:

$$\hat{\mu}^{\pm}(x,y)=\int_{-\infty}^{\infty}\sum_{n=1}^{2}B_n^{\pm}(\omega)M_n\mathrm{e}^{\mathrm{i}\omega x}\mathrm{d}\omega. \tag{33}$$

The general solutions of the homogeneous equations corresponding to Eq. (30) are written as

$$\begin{Bmatrix}\tilde{U}^{\pm}(\omega,y)\\\tilde{V}^{\pm}(\omega,y)\end{Bmatrix}=\sum_{n=1}^{4}A_n^{\pm}(\omega)\begin{Bmatrix}U_n\\V_n\end{Bmatrix}, \tag{34}$$

where $A_n^{\pm}(\omega)(n=1,2,3,4)$ are unknown functions, and the fundamental solutions are

$$\begin{cases} U_1 = \mathrm{e}^{-\omega y}, \\ V_1 = \mathrm{i}\mathrm{e}^{-\omega y}, \end{cases} \begin{cases} U_2 = y\mathrm{e}^{-\omega y}, \\ V_2 = \mathrm{i}(\chi/\omega + y)\mathrm{e}^{-\omega y}, \end{cases} \\ \begin{cases} U_3 = \mathrm{e}^{\omega y}, \\ V_3 = -\mathrm{i}\mathrm{e}^{\omega y}, \end{cases} \begin{cases} U_4 = y\mathrm{e}^{\omega y}, \\ V_4 = \mathrm{i}(\chi/\omega - y)\mathrm{e}^{\omega y}, \end{cases} \tag{35}$$

where $\chi = (\lambda_c + 3G)/(\lambda_c + G)$.

The special solutions of non-homogeneous equations Eq. (30) are assumed as

$$\begin{Bmatrix} U^{\pm}(\omega, y) \\ V^{\pm}(\omega, y) \end{Bmatrix} = \sum_{n=1}^{4} m_n^{\pm}(\omega, y) \begin{Bmatrix} U_n \\ V_n \end{Bmatrix}, \tag{36}$$

where $m_n^{\pm}(\omega, y)(n = 1, 2, 3, 4)$ are unknown functions. When the following conditions are met

$$\sum_{n=1}^{4} \frac{\partial m_n^{\pm}}{\partial y} U_n = 0, \ \sum_{n=1}^{4} \frac{\partial m_n^{\pm}}{\partial y} V_n = 0, \tag{37}$$

substituting them into Eq. (30) yields

$$\sum_{n=1}^{4} \frac{\partial m_n^{\pm}}{\partial y} \frac{\partial U_n}{\partial y} = \mathrm{i}\frac{3\eta K\omega}{NG}\left(B_1^{\pm}\mathrm{e}^{-\omega y} + B_2^{\pm}\mathrm{e}^{\omega y}\right), \\ \sum_{n=1}^{4} \frac{\partial m_n^{\pm}}{\partial y} \frac{\partial V_n}{\partial y} = \frac{3\eta K\omega}{N(\lambda_c + 2G)}\left(-B_1^{\pm}\mathrm{e}^{-\omega y} + B_2^{\pm}\mathrm{e}^{\omega y}\right). \tag{38}$$

According to Eqs. (37) and (38), $\frac{\partial m_n^{\pm}}{\partial y}(n = 1, 2, 3, 4)$ is easy to get, and then

$$\begin{Bmatrix} m_1^{\pm} \\ m_2^{\pm} \\ m_3^{\pm} \\ m_4^{\pm} \end{Bmatrix} = \alpha \begin{bmatrix} \chi y & y\mathrm{e}^{2\omega y} + \frac{G\mathrm{e}^{2\omega y}}{\omega(\lambda_c + G)} \\ 0 & -\mathrm{e}^{2\omega y} \\ -y\mathrm{e}^{-2\omega y} + \frac{G_0\mathrm{e}^{-2\omega y}}{\omega(\lambda_c + G)} & -\chi y \\ \mathrm{e}^{-2\omega y} & 0 \end{bmatrix} \begin{Bmatrix} B_1^{\pm} \\ B_2^{\pm} \end{Bmatrix}, \tag{39}$$

where $\alpha = -\mathrm{i}\frac{9\eta K(\lambda_c + G)}{4NG(\lambda_c + 2G)}$.

The general solutions of the non-homogeneous equations can be expressed as the superposition of the general solutions of the homogeneous equations and the special solutions of the non-homogeneous equations. So, the general solutions of Eq. (30) can be written as

$$\begin{Bmatrix} U^{\pm}(\omega, y) \\ V^{\pm}(\omega, y) \end{Bmatrix} = \sum_{n=1}^{4} \left[A_n^{\pm}(\omega) + m_n^{\pm}(\omega, y)\right] \begin{Bmatrix} U_n \\ V_n \end{Bmatrix}. \tag{40}$$

Using the inverse Fourier transform, we obtain the general solutions of displacements as

$$u^{\pm}(x, y) = \int_{-\infty}^{\infty} \sum_{n=1}^{4} \left(A_n^{\pm} + m_n^{\pm}\right) U_n \mathrm{e}^{\mathrm{i}\omega x} \mathrm{d}\omega, \\ v^{\pm}(x, y) = \int_{-\infty}^{\infty} \sum_{n=1}^{4} \left(A_n^{\pm} + m_n^{\pm}\right) V_n \mathrm{e}^{\mathrm{i}\omega x} \mathrm{d}\omega, \tag{41}$$

and the stresses as

$$\sigma_y^{\pm}(x, y) = \int_{-\infty}^{\infty} \sum_{n=1}^{4} \left(A_n^{\pm} + m_n^{\pm}\right) P_n \mathrm{e}^{\mathrm{i}\omega x} \mathrm{d}\omega \\ -\frac{3\eta K}{N} \int_{-\infty}^{\infty} \sum_{n=1}^{2} B_n^{\pm} M_n \mathrm{e}^{\mathrm{i}\omega x} \mathrm{d}\omega, \\ \sigma_{xy}^{\pm}(x, y) = \int_{-\infty}^{\infty} \sum_{n=1}^{4} \left(A_n^{\pm} + m_n^{\pm}\right) Q_n \mathrm{e}^{\mathrm{i}\omega x} \mathrm{d}\omega, \tag{42}$$

where $P_n(\omega, y) = \mathrm{i}\omega\lambda_c U_n + (\lambda_c + 2G)\frac{\partial V_n}{\partial y}$, $Q_n(\omega, y) = G\frac{\partial U_n}{\partial y} + \mathrm{i}\omega G V_n$ Furthermore, the concentration is

$$c^{\pm} - c_0 = \frac{1}{N} \int_{-\infty}^{\infty} \sum_{n=1}^{2} B_n^{\pm} M_n \mathrm{e}^{\mathrm{i}\omega x} \mathrm{d}\omega + \frac{3\eta K}{N} \\ \times \int_{-\infty}^{\infty} \sum_{n=1}^{4} \left[\left(A_n^{\pm} + m_n^{\pm}\right)\left(\mathrm{i}\omega U_n + \frac{\partial V_n}{\partial y}\right) + \frac{\partial m_n^{\pm}}{\partial y} V_n\right] \mathrm{e}^{\mathrm{i}\omega x} \mathrm{d}\omega. \tag{43}$$

3.2 Singular integral equations

To obtain the singular integral equations, we introduce the following dislocation density functions:

$$g_1(x) = \frac{\partial}{\partial x}[\hat{\mu}^{+}(x, 0) - \hat{\mu}^{-}(x, 0)], \tag{44}$$

$$g_2(x) = \frac{\partial}{\partial x}[u^{+}(x, 0) - u^{-}(x, 0)], \tag{45}$$

$$g_3(x) = \frac{\partial}{\partial x}[v^{+}(x, 0) - v^{-}(x, 0)]. \tag{46}$$

According to Eqs. (23) and (27), $g_n(x) = 0(|x| \geq l)$.

For the chemical boundary conditions Eqs. (25)-(27) and (44), we get the following equations for determining the unknown coefficients $B_n^{\pm}(\omega)(n = 1, 2)$:

$$\sum_{n=1}^{2} B_n^{+} M_n(\omega, b) = 0, \ \sum_{n=1}^{2} B_n^{-} M_n(\omega, -a) = 0, \tag{47}$$

$$\sum_{n=1}^{2}\left(B_n^{+}-B_n^{-}\right)\frac{\partial M_n(\omega,0)}{\partial y}=0,$$
$$\sum_{n=1}^{2}\left(B_n^{+}-B_n^{-}\right)M_n(\omega,0)=-\frac{\mathrm{i}}{2\pi\omega}\int_{-l}^{l}g_1(s)\mathrm{e}^{-\mathrm{i}\omega s}\mathrm{d}s. \tag{48}$$

For the mechanical boundary conditions Eqs. (21)-(23), (45), and (46), we get the following equations for determining the unknown coefficients $A_n^{\pm}(\omega)(n=1,2,3,4)$:

$$\sum_{n=1}^{4}\left[A_n^{+}+m_n^{+}(\omega,b)\right]P_n(\omega,b)=0,$$
$$\sum_{n=1}^{4}\left[A_n^{-}+m_n^{-}(\omega,-a)\right]P_n(\omega,-a)=0, \tag{49}$$

$$\sum_{n=1}^{4}\left[A_n^{+}+m_n^{+}(\omega,b)\right]Q_n(\omega,b)=0,$$
$$\sum_{n=1}^{4}\left[A_n^{-}+m_n^{-}(\omega,-a)\right]Q_n(\omega,-a)=0, \tag{50}$$

$$\sum_{n=1}^{4}\left[A_n^{+}-A_n^{-}+m_n^{+}(\omega,0)-m_n^{-}(\omega,0)\right]P_n(\omega,0)$$
$$-\frac{3\eta K}{N}\sum_{n=1}^{2}\left(B_n^{+}-B_n^{-}\right)M_n(\omega,0)=0, \tag{51}$$

$$\sum_{n=1}^{4}\left[A_n^{+}-A_n^{-}+m_n^{+}(\omega,0)-m_n^{-}(\omega,0)\right]Q_n(\omega,0)=0, \tag{52}$$

$$\sum_{n=1}^{4}\left[A_n^{+}-A_n^{-}+m_n^{+}(\omega,0)-m_n^{-}(\omega,0)\right]U_n(\omega,0)$$
$$=-\frac{\mathrm{i}}{2\pi\omega}\int_{-l}^{l}g_2(s)\mathrm{e}^{-\mathrm{i}\omega s}\mathrm{d}s, \tag{53}$$

$$\sum_{n=1}^{4}\left[A_n^{+}-A_n^{-}+m_n^{+}(\omega,0)-m_n^{-}(\omega,0)\right]V_n(\omega,0)$$
$$=-\frac{\mathrm{i}}{2\pi\omega}\int_{-l}^{l}g_3(s)\mathrm{e}^{-\mathrm{i}\omega s}\mathrm{d}s. \tag{54}$$

Combining the boundary conditions Eqs. (24) and (28), the following integral equations are obtained:

$$\frac{1}{2\pi}\int_{-l}^{l}\int_{-\infty}^{\infty}K_{11}(\omega)g_1(s)\mathrm{e}^{\mathrm{i}\omega(x-s)}\mathrm{d}\omega\mathrm{d}s=(k^*-1)j_0,$$
$$\frac{1}{2\pi}\int_{-l}^{l}\int_{-\infty}^{\infty}\sum_{k=1}^{3}K_{2k}(\omega)g_k(s)\mathrm{e}^{\mathrm{i}\omega(x-s)}\mathrm{d}\omega\mathrm{d}s=-p(x),$$
$$\frac{1}{2\pi}\int_{-l}^{l}\int_{-\infty}^{\infty}\sum_{k=1}^{3}K_{3k}(\omega)g_k(s)\mathrm{e}^{\mathrm{i}\omega(x-s)}\mathrm{d}\omega\mathrm{d}s=-q(x), \tag{55}$$
$$|x|<l,$$

where $K_{11}(\omega)$ and $K_{ij}(\omega)(i=2,3;j=1,2,3)$ are expressions in terms of ω.

To ensure the accuracy of the solutions, further transformation is required to isolate the Cauchy type integral kernel. Define $k_{ij}=\mathrm{Im}\left[\lim_{\omega\to+\infty}K_{ij}(\omega)\right]$, we get

$$k_{11}=\frac{1}{2},\ k_{23}=\frac{G(\lambda_c+G)}{\lambda_c+2G},\ k_{32}=\frac{G(\lambda_c+G)}{\lambda_c+2G},$$
$$k_{21}=k_{22}=k_{31}=k_{33}=0, \tag{56}$$

and the integral formula $\int_0^{\infty}\sin\omega s\cos\omega x\mathrm{d}\omega=\frac{1}{2}\left(\frac{1}{s+x}+\frac{1}{s-x}\right)$ [30] is used. And we find that $K_{ij}(\omega)$ has the following properties: $K_{11}(\omega)$, $K_{21}(\omega)$, $K_{23}(\omega)$, and $K_{32}(\omega)$ are odd functions and imaginary numbers; $K_{22}(\omega)$, $K_{31}(\omega)$, and $K_{33}(\omega)$ are even functions and real numbers. Then Eq. (55) can be simplified as

$$\frac{1}{\pi}\int_{-l}^{l}\left(\frac{k_{11}}{s-x}+Q_{11}\right)g_1(s)\mathrm{d}s=(k^*-1)j_0,$$
$$\frac{1}{\pi}\int_{-l}^{l}\left[\left(\frac{k_{23}}{s-x}+Q_{23}\right)g_3(s)+Q_{22}g_2(s)\right]\mathrm{d}s$$
$$=-p(x)-p_c(x), \tag{57}$$
$$\frac{1}{\pi}\int_{-l}^{l}\left[\left(\frac{k_{32}}{s-x}+Q_{32}\right)g_2(s)+Q_{33}g_3(s)\right]\mathrm{d}s$$
$$=-q(x)-q_c(x),\quad |x|<l,$$

where

$$Q_{11}(s,x)=-\int_0^{\infty}(\mathrm{Im}K_{11}-k_{11})\sin\omega(x-s)\mathrm{d}\omega, \tag{58}$$

$$Q_{22}(s,x)=\int_0^{\infty}\mathrm{Re}K_{22}\cos\omega(x-s)\mathrm{d}\omega,$$
$$Q_{23}(s,x)=-\int_0^{\infty}(\mathrm{Im}K_{23}-k_{23})\sin\omega(x-s)\mathrm{d}\omega, \tag{59}$$

$$Q_{32}(s,x)=-\int_0^{\infty}(\mathrm{Im}K_{32}-k_{32})\sin\omega(x-s)\mathrm{d}\omega,$$
$$Q_{33}(s,x)=\int_0^{\infty}\mathrm{Re}K_{33}\cos\omega(x-s)\mathrm{d}\omega, \tag{60}$$

$$Q_{21}(s,x)=-\int_0^{\infty}\mathrm{Im}K_{21}\sin\omega(x-s)\mathrm{d}\omega,$$
$$p_c(x)=\frac{1}{\pi}\int_{-l}^{l}Q_{21}(s,x)g_1(s)\mathrm{d}s, \tag{61}$$

$$Q_{31}(s,x)=\int_0^{\infty}\mathrm{Re}K_{31}\cos\omega(x-s)\mathrm{d}\omega,$$
$$q_c(x)=\frac{1}{\pi}\int_{-l}^{l}Q_{31}(s,x)g_1(s)\mathrm{d}s. \tag{62}$$

The above three equations are Cauchy type singular integral equations of the first kind. $p_c(x)$ and $q_c(x)$ can be considered as "equivalent diffusion stresses". That is, the stress intensity factors generated by the chemical loads are the same as that produced by acting $p_c(x)$ and $q_c(x)$ on the crack faces. According to the chemical loads, we know that $g_1(s)$ is an odd function, so that $p_c(x)$ and $q_c(x)$ are odd and even functions, respectively.

3.3 Numerical integration method

By introducing $\bar{s}=s/l$ and $\bar{x}=x/l$, the singular integral

equations can be transformed into standard form

$$\begin{aligned}
&\frac{1}{\pi}\int_{-1}^{1}\left(\frac{k_{11}}{\tilde{s}-\tilde{x}}+R_{11}\right)h_1(\tilde{s})\mathrm{d}\tilde{s}=(k^*-1)j_0,\\
&\frac{1}{\pi}\int_{-1}^{1}\left[\left(\frac{k_{23}}{\tilde{s}-\tilde{x}}+R_{23}\right)h_3(\tilde{s})+R_{21}h_1(\tilde{s})+R_{22}h_2(\tilde{s})\right]\mathrm{d}\tilde{s}\\
&=-p(l\tilde{x}),\\
&\frac{1}{\pi}\int_{-1}^{1}\left[\left(\frac{k_{32}}{\tilde{s}-\tilde{x}}+R_{32}\right)h_2(\tilde{s})+R_{31}h_1(\tilde{s})+R_{33}h_3(\tilde{s})\right]\mathrm{d}\tilde{s}\\
&=-q(l\tilde{x}),\quad |\tilde{x}|<1,
\end{aligned}\tag{63}$$

where $h_i(\tilde{s})=g_i(l\tilde{s})$ and $R_{ij}(\tilde{s},\tilde{x})=lQ_{ij}(l\tilde{s},l\tilde{x})$. The solutions of the Cauchy singular integral equations can be expressed as [31]

$$h_i(\tilde{s})=\frac{f_i(\tilde{s})}{\sqrt{1-\tilde{s}^2}},\tag{64}$$

where $f_i(\tilde{s})$ is continuous and bound in $|\tilde{s}|<1$ and non-zero at the endpoints $|\tilde{s}|=1$. To guarantee the existence of Cauchy principal value integral, the Hölder condition needs to meet

$$\left|h_i(\tilde{s})-h_i(\tilde{x})\right|\le d|\tilde{s}-\tilde{x}|^{\beta},\ |\tilde{s}|\le 1,\ |\tilde{x}|\le 1,\tag{65}$$

where d is a non-negative real constant, and $\beta\in(0,1]$ is an exponent.

The above three Cauchy type singular integral equations can be solved numerically by the Lobatto-Chebyshev method, and we can finally discretize Eq. (63) into a system of linear algebraic equations [32]:

$$\begin{aligned}
&\sum_{j=0}^{m}\frac{\lambda_j k_{11}f_1(\tilde{s}_j)}{\tilde{s}_j-\tilde{x}_k}+\sum_{j=0}^{m}\lambda_j R_{11}f_1(\tilde{s}_j)=m(k^*-1)j_0,\\
&\sum_{j=0}^{m}\frac{\lambda_j k_{23}f_3(\tilde{s}_j)}{\tilde{s}_j-\tilde{x}_k}+\sum_{j=0}^{m}\lambda_j\left[R_{21}f_1(\tilde{s}_j)\right.\\
&\left.+R_{22}f_2(\tilde{s}_j)+R_{23}f_3(\tilde{s}_j)\right]=-mp(l\tilde{x}_k),\\
&\sum_{j=0}^{m}\frac{\lambda_j k_{32}f_2(\tilde{s}_j)}{\tilde{s}_j-\tilde{x}_k}+\sum_{j=0}^{m}\lambda_j\left[R_{31}f_1(\tilde{s}_j)\right.\\
&\left.+R_{32}f_2(\tilde{s}_j)+R_{33}f_3(\tilde{s}_j)\right]=-mq(l\tilde{x}_k),
\end{aligned}\tag{66}$$

$$\sum_{j=0}^{m}\lambda_j f_1(\tilde{s}_j)=0,\ \sum_{j=0}^{m}\lambda_j f_2(\tilde{s}_j)=0,\ \sum_{j=0}^{m}\lambda_j f_3(\tilde{s}_j)=0,\tag{67}$$

where the discrete points

$$\begin{aligned}
&\tilde{s}_j=\cos(j\pi/m),\ (j=0,1,\cdots,m),\\
&\tilde{x}_k=\cos[(2k-1)\pi/(2m)],\ (k=1,2,\cdots,m),
\end{aligned}\tag{68}$$

with the corresponding weights given by $\lambda_0=\lambda_m=1/2$, $\lambda_1=\cdots=\lambda_{m-1}=1$. The above Eqs. (66) and (67) contain $3m+3$ algebraic equations and meanwhile $3m+3$ unknown constants $f_i(\tilde{s}_j)$ $(i=1,2,3;j=0,1,\cdots,m)$. As the number of discrete points increases, the calculated results will gradually converge. The numerical convergence appears to be very good for small values of m, so m is taken to be 30 in this paper.

4. Field quantities near the crack

To characterize the stress field near the crack tip, the stress intensity factors (SIFs) are defined as

$$\begin{aligned}
&K_{\mathrm{I}}=\lim_{x\to l^+}\sigma_y(x,0)\sqrt{2\pi(x-l)},\\
&K_{\mathrm{II}}=\lim_{x\to l^+}\sigma_{xy}(x,0)\sqrt{2\pi(x-l)},
\end{aligned}\tag{69}$$

where $\sigma_y=\sigma_y^{\mathrm{I}}+\sigma_y^{\mathrm{II}}$ and $\sigma_{xy}=\sigma_{xy}^{\mathrm{I}}+\sigma_{xy}^{\mathrm{II}}$. σ_y^{I} is non-singular, and according to Eq. (63),

$$\begin{aligned}
\sigma_y^{\mathrm{II}}(x,0)=\frac{1}{\pi}\int_{-1}^{1}&\left[\left(\frac{k_{23}}{\tilde{s}-\tilde{x}}+R_{23}\right)\frac{f_3(\tilde{s})}{\sqrt{1-\tilde{s}^2}}\right.\\
&\left.+R_{21}\frac{f_1(\tilde{s})}{\sqrt{1-\tilde{s}^2}}+R_{22}\frac{f_2(\tilde{s})}{\sqrt{1-\tilde{s}^2}}\right]\mathrm{d}\tilde{s}.
\end{aligned}\tag{70}$$

Moreover, σ_y^s is used to represent the singular part of σ_y^{II}, so we get

$$\lim_{x\to l^+}\sigma_y^s(x,0)=\frac{k_{23}}{\pi}\lim_{\tilde{x}\to 1^+}\int_{-1}^{1}\frac{f_3(\tilde{s})}{\tilde{s}-\tilde{x}}\frac{1}{\sqrt{1-\tilde{s}^2}}\mathrm{d}\tilde{s},\tag{71}$$

and then transform the formula as follows:

$$\begin{aligned}
\lim_{x\to l^+}\sigma_y^s(x,0)=&\frac{k_{23}}{\pi}\lim_{\tilde{x}\to 1^+}\int_{-1}^{1}\frac{f_3(\tilde{s})-f_3(\tilde{x})}{\tilde{s}-\tilde{x}}\frac{1}{\sqrt{1-\tilde{s}^2}}\mathrm{d}\tilde{s}\\
&-\frac{k_{23}}{\pi}\lim_{\tilde{x}\to 1^+}\int_{-1}^{1}\frac{f_3(\tilde{x})}{\tilde{s}-\tilde{x}}\frac{1}{\sqrt{1-\tilde{s}^2}}\mathrm{d}\tilde{s}.
\end{aligned}\tag{72}$$

According to Eq. (65), the first term of the above formula is non-singular, so it can be disregarded. For the second term, the following integral formula is employed:

$$\frac{1}{\pi}\int_{-1}^{1}\frac{1}{\tilde{s}-\tilde{x}}\frac{1}{\sqrt{1-\tilde{s}^2}}\mathrm{d}\tilde{s}=-\frac{1}{\sqrt{\tilde{x}^2-1}},\ \tilde{x}>1.\tag{73}$$

Combined with Eq. (69), we finally get $K_{\mathrm{I}}=-k_{23}f_3(1)\sqrt{\pi l}$. Similarly, we can get $K_{\mathrm{II}}=-k_{32}f_2(1)\sqrt{\pi l}$.

With the help of Eqs. (18) and (33), the chemical potential difference on the crack plane in the original problem is

$$\begin{aligned}
&\hat{\mu}^{\pm}(x,0)\\
&=\hat{\mu}^{\mathrm{I}}(x,0)-\frac{1}{\pi}\int_{-l}^{l}\int_{0}^{\infty}K_{41}^{\pm}(\omega)g_1(s)\sin\omega(x-s)\mathrm{d}\omega\mathrm{d}s,
\end{aligned}\tag{74}$$

where $K_{41}^{\pm}(\omega)$ are expressions in terms of ω. Combined with Eq. (66), it can be further expressed as

$$\hat{\mu}^{\pm}(l\tilde{x},0)=\hat{\mu}^{\mathrm{I}}(l\tilde{x},0)-\frac{1}{m}\sum_{j=0}^{m}\lambda_j R_{41}^{\pm}(\tilde{s}_j,\tilde{x})f_1(\tilde{s}_j),\tag{75}$$

where $R_{41}^{\pm}(\tilde{s},\tilde{x})=l\int_0^{\infty}K_{41}^{\pm}(\omega)\sin\omega l(\tilde{x}-\tilde{s})\mathrm{d}\omega$. According to

Eqs. (57) and (66), the equivalent diffusion stresses on the crack faces can be calculated numerically as

$$p_c(l\tilde{x}) = \frac{l}{m}\sum_{j=0}^{m}\lambda_j Q_{21}(l\tilde{s}, l\tilde{x}) f_1(\tilde{s}_j),$$
$$q_c(l\tilde{x}) = \frac{l}{m}\sum_{j=0}^{m}\lambda_j Q_{31}(l\tilde{s}, l\tilde{x}) f_1(\tilde{s}_j). \tag{76}$$

5. Numerical results and discussion

5.1 Chemical potential and equivalent diffusion stresses distribution

In this section, the effects of flux conductivity and geometric parameters on the distribution of chemical potential and equivalent diffusion stresses on the crack plane are studied. For the convenience of comparison, the following normalized chemical potential and concentration are used

$$\tilde{\mu}^{\pm}(x,0) = \frac{\tilde{\mu}^{\pm}(x,0) - \tilde{\mu}^{\mathrm{I}}(x,0)}{l j_0},$$
$$\tilde{c}^{\pm}(x,0) = N\frac{c^{\pm}(x,0) - c^{\mathrm{I}}(x,0)}{l j_0}. \tag{77}$$

Based on Eq. (8), we can define a parameter with the same dimension as stress $\sigma_{c0} = 3K\eta j_0 l / N$. Then the normalized equivalent diffusion stresses are defined as

$$\tilde{p}_c(x) = \frac{p_c(x)}{\sigma_{c0}},\ \tilde{q}_c(x) = \frac{q_c(x)}{\sigma_{c0}}. \tag{78}$$

The material parameters [23,33] used for the numerical calculations are given in Table 1.

Next, we present the numerical results for a special case with $a = b = l$. The normalized chemical potentials at the midpoint and tip of the crack under different flux conductivities k^* are shown in Fig. 3. The chemical potentials on the upper and lower crack faces are the same when the flux conductivity $k^* = 1$. That is, the fully permeable crack implies that a crack has no impact on the diffusion process. For other cases ($k^* \in [0, 1)$), there is a chemical potential jump on the crack face, especially at the crack tip. The influence of flux conductivity on the chemical potential of the crack face is linear, and the smaller the flux conductivity, the greater the chemical potential change on the crack face.

According to Eq. (57), the influence of flux conductivity on the singular integral equation only exists at the right side and is linear, so the influence on the chemical potential and the stress is linear. Therefore, in the following analysis, we only need to consider the case of $k^* = 0$. Then the diffusion flux on the crack face in subproblem II is $j_y = D_m j_0$.

Table 1 Values of material parameters

Material parameters	Notation	Value
Lame constant (GPa)	λ	1.154
Shear modulus (GPa)	G	0.769
Coefficient of chemical expansion (m^3/mol)	η	10^{-6}
Chemistry modulus (J m^3/mol^2)	N	1.5

Figures 4 and 5 present the distributions of chemical potential and concentration along the crack plane $y = 0$ under chemical loading with different layer thicknesses. As shown in Fig. 4, the normalized chemical potential on the upper crack face is greatly affected and gradually increases as the upper layer thickness increases, but the normalized chemical potential on the lower crack face is slightly affected. Under chemical loading, the concentration has a similar distribution to the chemical potential, as shown in Fig. 5. As the layer thickness increases, the normalized concentration on crack face increases.

Figure 6 gives the distribution of equivalent diffusion stresses along the crack plane $y = 0$ with different upper layer thicknesses for a fixed $a / l = 1$. The equivalent diffusion normal stress and shear stress are even function and odd

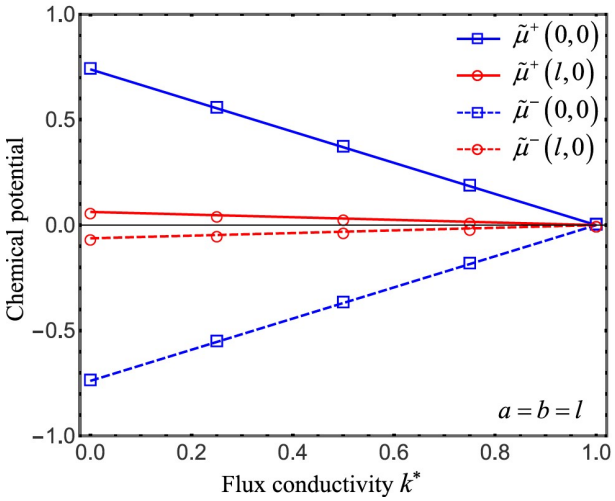

Figure 3 Effects of flux conductivity k^* on the chemical potentials at the midpoint and tip of the crack ($a = b = l$).

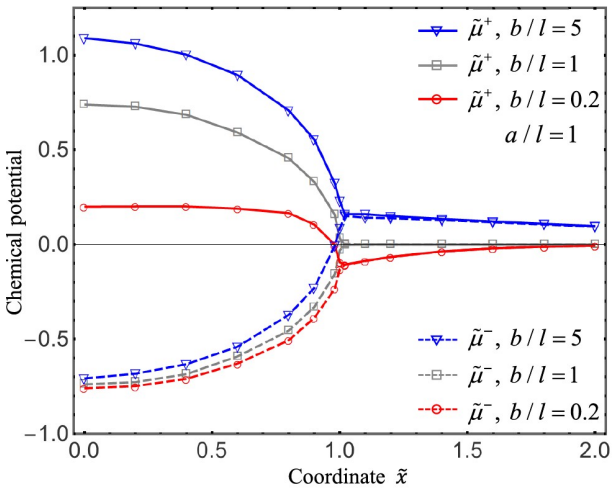

Figure 4 The distribution of chemical potential along the crack plane with different upper layer thickness b / l =0.2, 1, 5 for a fixed a / l = 1.

function, respectively, as can be seen in Fig. 6. The equivalent diffusion shear stress is greater than the equivalent diffusion normal stress. The equivalent shear stress increases with respect to the upper layer thickness.

5.2 Stress singularity under chemo-mechanical loading

The normalized stress intensity factors (NSIF) are defined as

$$\widetilde{K}_{\mathrm{I}}=\frac{K_{\mathrm{I}}}{\sigma_{c0}\sqrt{\pi l}},\ \widetilde{K}_{\mathrm{II}}=\frac{K_{\mathrm{II}}}{\sigma_{c0}\sqrt{\pi l}}. \tag{79}$$

Assuming that the crack propagation direction is along the x-axis, the normalized energy release rate (NERR) can be obtained as

$$\widetilde{G}_c=\widetilde{K}_{\mathrm{I}}^2+\widetilde{K}_{\mathrm{II}}^2. \tag{80}$$

In this section, the effects of loads and geometric parameters on the NSIF and NERR under chemical and mechanical loads are studied. Based on the above analysis of chemical potential, some special cases of crack face stresses $p(x)$ and $q(x)$ in subproblem II are explored:

(1) Case of pure chemical loading: $p(x)=q(x)=0$

When the crack face normal stress and shear stress are zero, the stress intensity factors induced by pure chemical loading ($j_y=D_m j_0$) are studied. Figure 7 shows the effects of crack geometric location on the stress intensity factors with different strip thicknesses $a+b=2l$ and $a+b=20l$. In general, the chemical load induces both mode I and mode II SIFs. However, when $a=b$, $\widetilde{K}_{\mathrm{I}}$ is zero but $\widetilde{K}_{\mathrm{II}}$ is non-zero. This indicates that the chemical load only results in mode II SIF when the crack is in the mid-plane of the strip.

As the upper layer thickness gradually increases, $\widetilde{K}_{\mathrm{I}}$ decreases and changes from positive to negative values, and $\widetilde{K}_{\mathrm{II}}$ increases first and then decreases. The negative $\widetilde{K}_{\mathrm{I}}$ means that it is possible to have crack face interference [29], and the corresponding solutions given are not valid. In such cases, the contact of the crack faces would occur, so that the normal stress near the crack tip is negative and the crack face is in a state of compression together with in-plane shear. The negative and positive $\widetilde{K}_{\mathrm{II}}$ means that the shear stress at the crack tip can change direction in some cases.

It can be seen that $\widetilde{K}_{\mathrm{I}}$ and $\widetilde{K}_{\mathrm{II}}$ show odd symmetry and even symmetry with respect to the mid-plane of the strip, respectively. The absolute value of the stress intensity factors in the case of $a+b=20l$ is smaller than those in the case of $a+b=2l$. This indicates that the strip thickness has a great effect on SIFs, and an increase in thickness leads to a decrease in the magnitude of SIFs induced by chemical loading.

(2) Case with crack face normal stress: $p(x)=k_0\sigma_{c0}$, $q(x)=0$

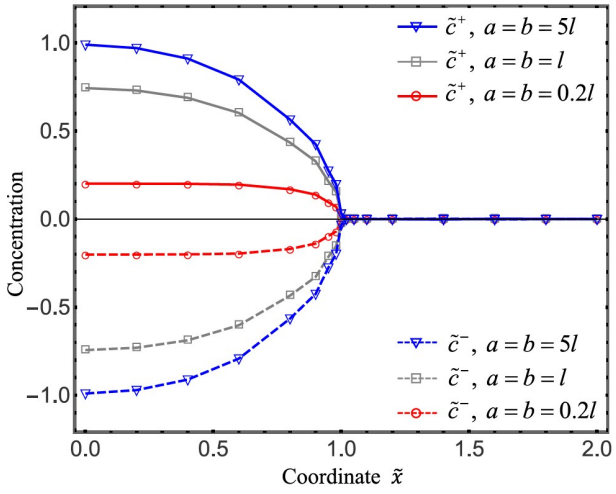

Figure 5 The distribution of concentration along the crack plane with different layer thickness $a=b=0.2l$, l, $5l$.

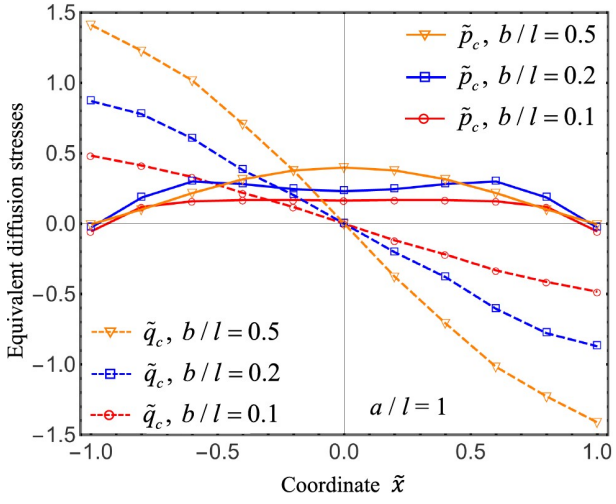

Figure 6 The distribution of the equivalent diffusion normal stress $\tilde{p}_c(l\bar{x})$ and shear stress $\tilde{q}_c(l\bar{x})$ on the crack face with different upper layer thickness $b/l=0.1$, 0.2, 0.5 for a fixed $a/l=1$.

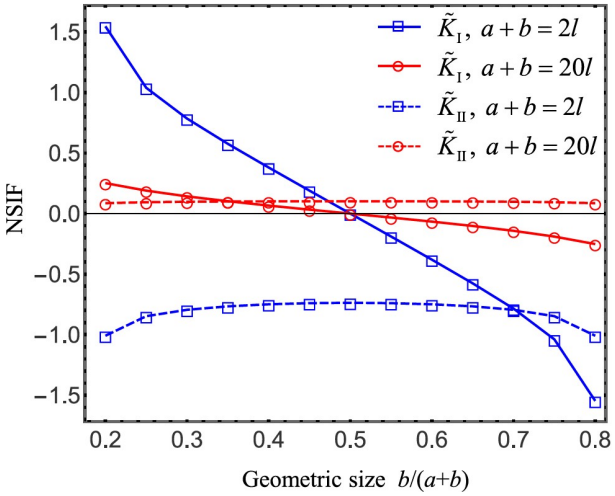

Figure 7 Effects of crack geometric location on stress intensity factors induced by chemical loading.

The crack face shear stress is zero, and the normal stress is uniformly distributed as $p(x) = k_0\sigma_{c0}$, where k_0 is the load factor and represents the magnitude relationship between chemical loads and mechanical loads. The crack tip stress field is mainly affected by the chemical loads for the case of small $|k_0|$. However, it is mainly affected by the mechanical loads for large $|k_0|$, and it is affected by both chemical and mechanical loads for other cases.

The effects of the crack face normal stress on stress intensity factors for a fixed $a/l = 1$ are given in Fig. 8a. For the case $b/l = 0.2$, $\widetilde{K}_{\mathrm{I}}$ and $\widetilde{K}_{\mathrm{II}}$ linearly increase and decrease respectively as k_0 increases. This is, the normal stress can induce both mode I and mode II SIFs in general. However, for the special case $a = b$, $\widetilde{K}_{\mathrm{I}}$ increases linearly as k_0 increases, but $\widetilde{K}_{\mathrm{II}}$ is not affected. This indicates that when the crack is in the mid-plane of the strip, the normal stress only results in mode I SIF.

Illustrated in Fig. 8a, as the upper layer thickness increases, the slope of the solid line $\widetilde{K}_{\mathrm{I}}$ gradually decreases and approaches the dot-dashed line, which has the expression $\widetilde{K}_{\mathrm{I}} = k_0$, and this is consistent with the mode I crack problem in linear elastic fracture mechanics (LEFM). As shown in Fig. 8b, the energy release rate is not symmetrically distributed in the case $b/l = 0.2$, but symmetrically distributed in the special case $a = b$. The smaller the upper layer thickness, the greater the energy release rate. This indicates that the crack geometric location has a great effect on the energy release rate: the NERR increases rather rapidly as the crack approaches the strip surface.

(3) Case with crack face shear stress: $p(x) = 0$, $q(x) = k_0\sigma_{c0}$

The crack face normal stress is zero, and the shear stress is uniformly distributed as $q(x) = k_0\sigma_{c0}$, where k_0 is the load factor. The effects of the crack face shear stress on stress intensity factors are given in Fig. 9a. For the case $b/l = 0.2$, both $\widetilde{K}_{\mathrm{I}}$ and $\widetilde{K}_{\mathrm{II}}$ linearly increase with respect to k_0. That is, the shear stress can affect both mode I and mode II SIFs. However, for the special case $a = b$, $\widetilde{K}_{\mathrm{I}}$ remains zero, but $\widetilde{K}_{\mathrm{II}}$ linearly increases as k_0 increases. This indicates that the shear stress only results in mode II SIF when the crack is in the mid-plane of the strip.

As the upper layer thickness increases, the slope of the dashed line $\widetilde{K}_{\mathrm{II}}$ gradually decreases and approaches the dot-dashed line, which has the expression $\widetilde{K}_{\mathrm{II}} = k_0$, and this is

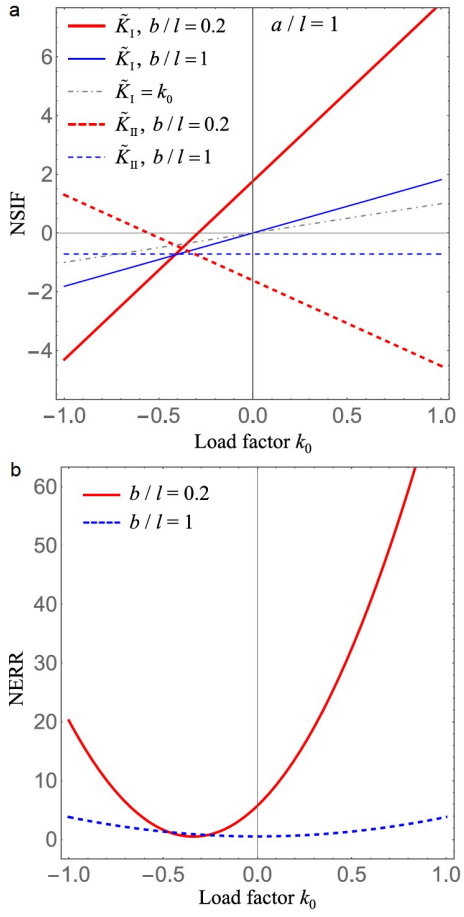

Figure 8 Effects of the crack face normal stress on **a** stress intensity factors and **b** energy release rate.

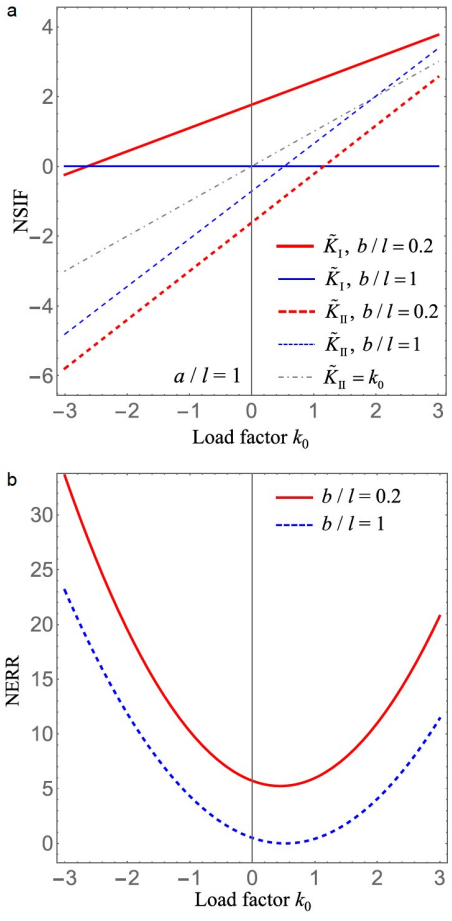

Figure 9 Effects of the crack face shear stress on **a** stress intensity factors and **b** energy release rate.

consistent with the mode II crack problem in LEFM. The energy release rate is not symmetrically distributed for both the case $b/l = 0.2$ and $a = b$, as shown in Fig. 9b. The smaller the upper layer thickness, the greater the energy release rate.

In summary, the stress field near the crack tip is affected by the chemical loads, mechanical loads (normal stress or shear stress), and geometric configuration, thus the stress singularity at the crack tip is usually a mixture of mode I and mode II types. The numerical results reveal that the SIFs can be either positive or negative depending on the combination of the chemical and mechanical loads. For a certain load factor, mode II (or mode I) SIF could be zero, that is, only a pure mode I (or mode II) SIF is generated.

(4) A limit case: $a = b \to \infty$

When the geometric size $a = b$ increases gradually, we studied the change of stress intensity factors induced by four crack face loads in subproblem II: (i) chemical load $j_y = D_m j_0$, (ii) constant normal stress $p(x) = \sigma_{c0}$, (iii) constant shear stress $q(x) = \sigma_{c0}$, (iv) shear stress $q(x) = \sigma_{c0}x$.

As the geometric size $a = b \to \infty$, numerical results show that $\widetilde{K}_{\mathrm{II}}$ induced by the chemical load approaches to zero. Therefore, the other non-zero stress intensity factors approach a limit value respectively, as shown in Fig. 10:

$$\begin{aligned} &\widetilde{K}_{\mathrm{I}} \to 1, && \text{for } p(x) = \sigma_{c0}, \\ &\widetilde{K}_{\mathrm{II}} \to 1, && \text{for } q(x) = \sigma_{c0}, \\ &\widetilde{K}_{\mathrm{II}} \to 0.5, && \text{for } q(x) = \sigma_{c0}x. \end{aligned} \tag{81}$$

These results are consistent with the SIFs of mode I and mode II crack in LEFM, which validate the theoretical derivation and the numerical calculation procedure in this paper.

6. Summary and conclusions

This paper studies a plane crack problem in a strip subjected to chemo-mechanical loading under steady state diffusion.

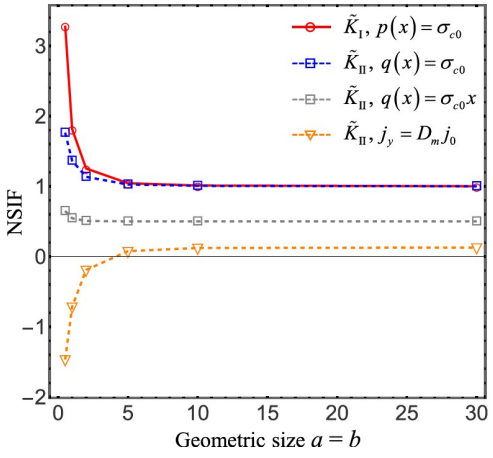

Figure 10 Effects of the geometric size $a = b$ on stress intensity factors under different loading.

Using the Fourier transform and dislocation density functions, the crack problem is reduced to a set of singular integral equations, which are solved numerically by the Lobatto-Chebyshev method. By analyzing the chemical potential distribution and stress field near the crack, the following conclusions can be drawn. The influence of flux conductivity on the chemical potential of the crack face is linear, and there is a change of chemical potential on the crack face in general. Affected by the chemical loads, mechanical loads (normal stress or shear stress), and geometric configuration, the stress singularity at the crack tip is usually a mixture of mode I and mode II types. The crack geometric location has a great effect on the stress intensity factors and energy release rate. As the strip thickness gradually increases, the stress intensity factors approach the classical results in LEFM.

This work was supported by the National Natural Science Foundation of China (Grant Nos. 11932005 and 11772106).

1 O. Coussy, Poromechanics (John Wiley & Sons, England, 2004).
2 S. A. Chester, A constitutive model for coupled fluid permeation and large viscoelastic deformation in polymeric gels, Soft Matter **8**, 8223 (2012).
3 N. Swaminathan, J. Qu, and Y. Sun, An electrochemomechanical theory of defects in ionic solids. Part II. Examples, Philos. Mag. **87**, 1723 (2007).
4 Z. Cui, F. Gao, and J. Qu, A finite deformation stress-dependent chemical potential and its applications to lithium ion batteries, J. Mech. Phys. Solids **60**, 1280 (2012).
5 S. Cai, and Z. Suo, Mechanics and chemical thermodynamics of phase transition in temperature-sensitive hydrogels, J. Mech. Phys. Solids **59**, 2259 (2011).
6 R. Marcombe, S. Cai, W. Hong, X. Zhao, Y. Lapusta, and Z. Suo, A theory of constrained swelling of a pH-sensitive hydrogel, Soft Matter **6**, 784 (2010).
7 J. S. Katz, and J. A. Burdick, Light-responsive biomaterials: development and applications, Macromol. Biosci. **10**, 339 (2010).
8 H. Yang, and J. Qu, Fracture toughness of LixSi alloys in lithium ion battery, Extreme Mech. Lett. **32**, 100555 (2019).
9 L. S. Bennethum, M. A. Murad, and J. H. Cushman, Modified Darcy's law, Terzaghi's effective stress principle and Fick's law for swelling clay soils, Comput. Geotechnics **20**, 245 (1997).
10 M. A. Biot, General theory of three-dimensional consolidation, J. Appl. Phys. **12**, 155 (1941).
11 W. Hong, X. Zhao, J. Zhou, and Z. Suo, A theory of coupled diffusion and large deformation in polymeric gels, J. Mech. Phys. Solids **56**, 1779 (2008).
12 L. Anand, 2014 Drucker medal paper: A derivation of the theory of linear poroelasticity from chemoelasticity, J. Appl. Mech. **82**, 111005 (2015).
13 Q. Yang, Q. Qin, L. Ma, X. Lu, and C. Cui, A theoretical model and finite element formulation for coupled thermo-electro-chemo-mechanical media, Mech. Mater. **42**, 148 (2010).
14 L. Ma, and Q. Yang, in Transient modeling on the coupled chemo-mechanical behaviors of hydrogels in an aqueous environment: Proceedings of SPIE 8409, Third International Conference on Smart Materials and Nanotechnology in Engineering, Shenzhen, 2011.
15 S. A. Chester, C. V. Di Leo, and L. Anand, A finite element implementation of a coupled diffusion-deformation theory for elasto-

meric gels, Int. J. Solids Struct. **52**, 1 (2015).
16 P. D. Zarnas, B. L. Boyce, J. Qu, and R. Dingreville, Stress-induced transition from vacancy annihilation to void nucleation near microcracks, Int. J. Solids Struct. **213**, 103 (2021).
17 J. Christensen, and J. Newman, Stress generation and fracture in lithium insertion materials, J. Solid State Electrochem. **10**, 293 (2006).
18 H. Haftbaradaran, and J. Qu, Two-dimensional chemo-elasticity under chemical equilibrium, Int. J. Solids Struct. **56-57**, 126 (2015).
19 X. Gao, D. Fang, and J. Qu, A chemo-mechanics framework for elastic solids with surface stress, Proc. R. Soc. A. **471**, 20150366 (2015).
20 P. L. Bishay, J. Sladek, N. Fabry, V. Sladek, and C. Zhang, Perturbation finite element solution for chemo-elastic boundary value problems under chemical equilibrium, Acta Mech. Sin. **35**, 981 (2019).
21 C. Xu, M. K. Mudunuru, and K. B. Nakshatrala, Material degradation due to moisture and temperature. Part 1: mathematical model, analysis, and analytical solutions, Continuum Mech. Thermodyn. **28**, 1847 (2016).
22 X. Zhang, and Z. Zhong, A thermodynamic framework for thermo-chemo-elastic interactions in chemically active materials, Sci. China-Phys. Mech. Astron. **60**, 084611 (2017).
23 X. Zhang, and Z. Zhong, A coupled theory for chemically active and deformable solids with mass diffusion and heat conduction, J. Mech. Phys. Solids **107**, 49 (2017).
24 Z. Zhong, B. Qin, and J. Chen, A coupled theory for soft materials at finite strain with heat conduction, diffusion and chemical reactions, Comput. Mater. Sci. **188**, 110189 (2021).
25 H. Haftbaradaran, and J. Qu, A path-independent integral for fracture of solids under combined electrochemical and mechanical loadings, J. Mech. Phys. Solids **71**, 1 (2014).
26 M. Zhang, J. Qu, and J. R. Rice, Path independent integrals in equilibrium electro-chemo-elasticity, J. Mech. Phys. Solids **107**, 525 (2017).
27 N. Bouklas, and R. Huang, Swelling kinetics of polymer gels: comparison of linear and nonlinear theories, Soft Matter **8**, 8194 (2012).
28 Y. Yu, C. M. Landis, and R. Huang, Poroelastic effects on steady state crack growth in polymer gels under plane stress, Mech. Mater. **143**, 103320 (2020).
29 Y. Lee, and F. Erdogan, Interface cracking of FGM coatings under steady-state heat flow, Eng. Fract. Mech. **59**, 361 (1998).
30 Y. D. Li, and K. Y. Lee, Two collinear unequal cracks in a poled piezoelectric plane: Mode I case solved by a new approach of real fundamental solutions, Int. J. Fract. **165**, 47 (2010).
31 F. Erdogan, G. D. Gupta, and T. Cook, Numerical solution of singular integral equations. In: G. C. Sih, ed. Methods of Analysis and Solutions of Crack Problems (Noordhoff International Publishing, Leyden, 1973), pp. 368-425.
32 W. K. Binienda, and S. M. Arnold, Driving force analysis in an infinite anisotropic plate with multiple crack interactions, Int. J. Fract. **71**, 213 (1995).
33 I. Laresgoiti, S. Käbitz, M. Ecker, and D. U. Sauer, Modeling mechanical degradation in lithium ion batteries during cycling: Solid electrolyte interphase fracture, J. Power Sources **300**, 112 (2015).

化学-力学荷载下平面裂纹问题的断裂分析

时俊涛, 仲　政

摘要　基于线性的化学弹性模型, 本文给出了化学-力学荷载下平面裂纹问题的断裂分析. 引入流通系数来描述裂纹缺陷对扩散过程的影响. 利用傅里叶变换和位错密度函数, 裂纹问题被归结为一组奇异积分方程, 采用Lobatto-Chebyshev方法对其进行数值求解. 通过参数研究揭示了流通系数、几何构型、化学和力学载荷对裂纹尖端场的影响. 数值结果表明, 裂纹尖端的应力奇异性通常表现为I型和II型的混合.